# Total thermal neutron cross section measurements of yttrium hydride from 0.0005 - 3 eV

D. Fritz [a],[*], Y. Danon [a], M. Rapp [b], T.H. Trumbull [b], M. Zerkle [c], J. Holmes [c], C.W. Chapman [d], G. Arbanas [d], J.M. Brown [d], K. Ramic [d], X. Hu [e], S. Singh [a], A. Ney [a], P. Brain [a], K. Cook [a], B. Wang [a]

[a] *Gaerttner LINAC Center, Rensselaer Polytechnic Institute, Troy, NY 12180, USA*
[b] *Naval Nuclear Laboratory, P.O. Box 1072, Schenectady, NY 12301, USA*
[c] *Naval Nuclear Laboratory, PO Box 79, West Mifflin, PA 15122, USA*
[d] *Nuclear Energy and Fuel Cycle Division, Oak Ridge National Laboratory, Oak Ridge, TN 37830, USA*
[e] *Material Science and Technology Division, Oak Ridge National Laboratory, Oak Ridge, TN 37830, USA*

## ARTICLE INFO

## ABSTRACT

Yttrium hydride serves as a neutron moderator material that enables compact, high temperature nuclear reactors. However, in order to accurately design and simulate a nuclear system relying upon yttrium hydride, the fundamental nuclear data of yttrium hydride must be well understood. Thermal neutron scattering law (TSL) evaluations represent an important aspect of nuclear data as thermal scattering can drastically alter the neutron multiplication factor of a system. Therefore, to support evaluation and validation of thermal neutron scattering for yttrium hydride, researchers at Rensselaer Polytechnic Institute (RPI) performed total thermal neutron cross section measurements for $YH_{1.68}$ and $YH_{1.85}$ over the energy range of 0.0005 - 3 eV. These measurements represent the first total cross section measurements for yttrium hydride that encompass the entire thermal region. Comparisons were made against the ENDF-B/VIII.0, Zerkle & Holmes and Oak Ridge National Laboratory TSL evaluations, where generally good agreement was found.

## 1. Introduction

In the quest for compact nuclear reactors, moderator materials that can withstand high temperatures and provide a strong moderating ability are necessary. Hydrogen serves as the ideal moderator material due to its strong ability to down-scatter neutrons. To this end, metal hydrides, specifically yttrium hydride, provide a hydrogen dense alternative to metallic or ceramic moderators capable of withstanding high operating temperatures. The performance of yttrium hydride at high temperature has prompted the US Department of Energy (DOE) to investigate yttrium hydride moderators for the design of various compact reactor systems (Shivprasad et al., September 2020).

In order to accurately design a yttrium hydride moderated nuclear reactor the interactions of neutrons with yttrium hydride at the molecular level during the thermalization process must be well understood. More specifically, in the thermal region (<3 eV), the molecular bond effect must be accounted for as the wavelength (energies) of neutrons in this region become of similar magnitude to that of molecular excitations (e.g. rotations or vibrations) and collective excitations, known as phonons. To account for these molecular bond effects, transport codes such as MCNP (Werner et al., 2018) use thermal scattering law (TSL) evaluations.

TSL evaluations are based on a measured or calculated phonon spectrum of a material that represent the molecular motions that a material undergoes. These phonon spectra can be input into codes such as NJOY (Macfarlane et al., 2017) and FLASSH (Zhu and Hawari, 2018) where $S(\alpha, \beta)$ calculations are performed to generate a thermal scattering kernel that can be directly supplied to neutron transport codes, such as MCNP. However, these thermal scattering kernels need experimental validation in the form of total thermal neutron cross section measurements due to the large impact of thermal scattering on system criticality. This report details high accuracy total cross section measurements performed for yttrium hydride with a H/Y ratio of 1.85 and 1.68 in order to validate the ENDF-B/VIII.0 (Brown et al., 2018), Zerkle & Holmes (Z&H) (Zerkle et al., 2021) and ORNL (Chapman et al., 2020) TSL evaluations.

## 2. Overview of yttrium hydride

Yttrium hydride is produced by exposing $\alpha$-phase yttrium metal to a hydrogen atmosphere at high temperature and pressure, allowing for the formation of $\delta$-phase $YH_2$. However, yttrium hydride compositions

---

* Corresponding author.
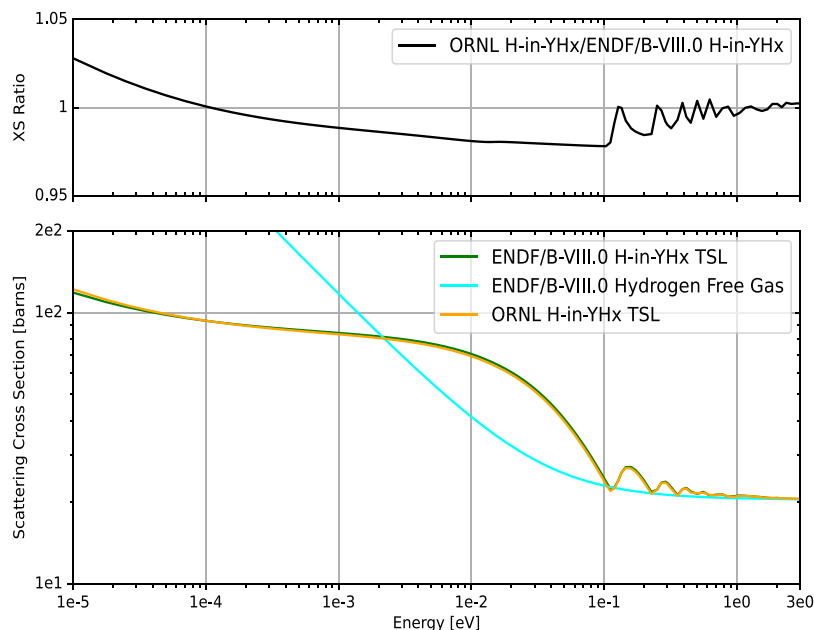   *E-mail address:* fritzd3@rpi.edu (D. Fritz).

**Fig. 1.** ENDF-B/VIII.0 (Brown et al., 2018) and ORNL (Chapman et al., 2020) thermal scattering cross section for the hydrogen component of yttrium hydride. The scattering cross section (XS) ratio of the ORNL H-in-YHx evaluation to the ENDF/B-VIII.0 evaluation is provided. Agreement within a few percent is seen between the two H-in-YHx evaluations.

of practical engineering interest at room temperature are a two phase solid solution of $YH_2$ and yttrium metal, with an H/Y ratio less than 2. Yttrium hydride has excellent thermal stability between 400 °C and 1000 °C, allowing for the material to operate in this temperature region with little to no removal of hydrogen from the yttrium hydride matrix. The ability of yttrium hydride to provide a significant and stable hydrogen concentration at high temperature makes it a material ideally suited for use in compact, high temperature reactors (Shivprasad et al., September 2020).

Before yttrium hydride can be used in nuclear reactor systems the underlying nuclear data must be rigorously tested. The molecular bonds that exist between hydrogen and yttrium in yttrium hydride dramatically alter the scattering cross section for both components in the thermal energy range as shown by Figs. 1 and 2 for hydrogen and yttrium, respectively. Here, the large discrepancy in scattering cross section between the various yttrium hydride thermal scattering law evaluations and the free gas model can be clearly seen. In addition, large differences in the coherent elastic scattering component (Bragg edges) are present between the ORNL and Z&H Y-in-YHx TSL evaluations. It should be noted that coherent elastic scattering contribution was added to the ORNL TSL evaluations given in Chapman et al. (2020). The NJOY+NCrystal tool was used to create the ORNL evaluations shown (Ramić et al., 2022). In addition, all TSL evaluations shown in Figs. 1 and 2 were processed using NJOY.

The hydrogen and yttrium scattering cross sections in yttrium hydride, as shown in Figs. 1 and 2, are then atomically mixed to prepare the total cross section of yttrium hydride for a given H/Y ratio. In the thermal energy range the total cross section consists of scattering and capture components, shown in Fig. 3. The total cross section is dominated by the scattering component in the thermal energy range, with the scattering cross section comprising 98% of the total at the thermal energy point (0.0253 eV). However, at extremely low neutron energies, the capture cross section becomes a larger component of the total cross section.

## 3. Experimental methods and materials

In order to validate thermal scattering kernel evaluations for yttrium hydride, neutron transmission measurements were performed to infer the total neutron cross section in the thermal energy region. To produce an intense neutron flux that could extend down to 0.0005 eV, the Enhanced Thermal Target (ETT) was coupled with a polyethylene based cold moderator system at the RPI LINAC facility. The Enhanced Thermal Target was designed to produce large amounts of thermal neutron flux and is suitable for measurements from 0.001–20 eV. The addition of a polyethylene based cold moderator system allows for the cross section measurement capability to be extended down to 0.0005 eV. Fig. 4 displays the excellent signal-to-background ratio present for the yttrium hydride measurements from the Enhanced Thermal Target + Cold Moderator (ETTC). For more information regarding the target and cold moderator system please see Fritz and Danon (2021) and Fritz and Danon (2020).

To detect the neutrons, a 3 mm thick (GS-20) lithium glass detector was placed approximately 15 m away from the target as shown in Fig. 5. The detector connects to a time of flight (TOF) clock via a pre-amplifier, amplifier, constant fraction discriminator, and level adapter. The TOF clock connects to a data acquisition computer to allow for autonomous data collection above 20 eV for this flight path. The LINAC generated 46 MeV electrons at a pulse repetition rate of 18 Hz and a pulse width of 628 ns. The TOF clock recorded data with a bin width of 409.6 ns. In addition to the samples, 0.95 cm of lead was placed in beam to reduce gamma background.

For the purpose of effectively measuring the yttrium hydride total cross section, four samples with a diameter of approximately 4.9 cm were selected: 5 mm and 2 mm thick samples with an H/Y of 1.85 and 5 mm and 2 mm thick samples with an H/Y of 1.68. For more information concerning the fabrication process and material properties of these samples, see Hu et al. (2020) and Hu and Terrani (2021). The physical dimensions of each sample were measured to calculate the areal density used in the calculation of cross section. These dimensions, and their associated uncertainty, are displayed in Table 1 where it can easily be seen that, in general, the relative uncertainty in the areal density is very small.

Upon sample inspection, the thickness of the 2 mm, $YH_{1.85}$ sample was not uniform, with the thickness increasing when moving away from the sample center. When a sample is placed on the sample changer, the neutron beam only passes through the interior area of the sample, not the entire area. Therefore, the increasing thickness suggests that the measured areal density for a uniform thickness was higher than that seen by the neutron beam. In order to find the true areal density to use,
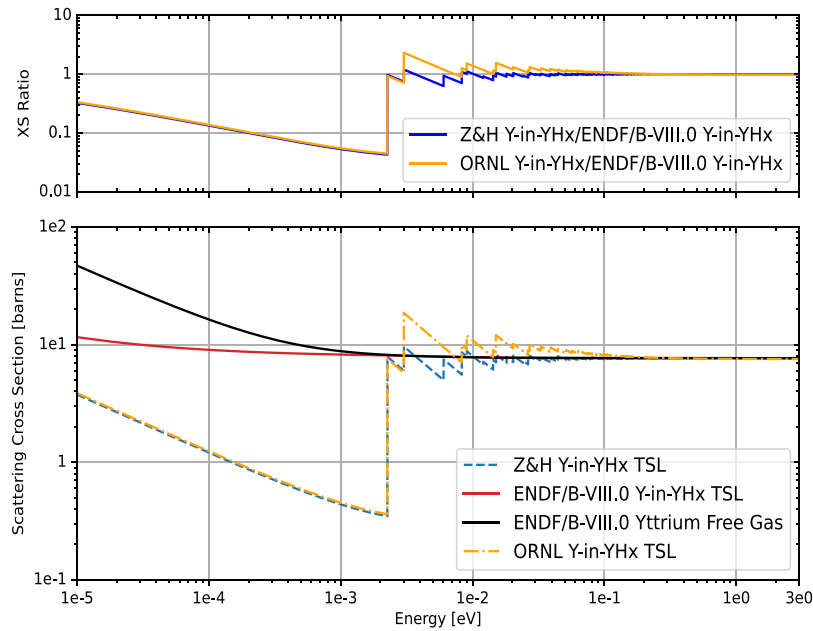
**Fig. 2.** ENDF-B/VIII.0 (Brown et al., 2018; Zerkle et al., 2021), and ORNL (Chapman et al., 2020) thermal scattering cross section for the yttrium component of yttrium hydride. The scattering cross section (XS) ratio of the ORNL and Z&H Y-in-YHx evaluations to the ENDF/B-VIII.0 evaluation is provided, where large differences are seen.
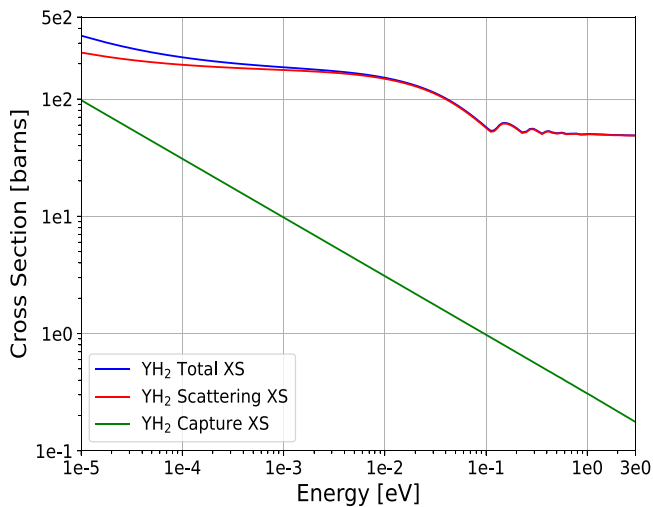


**Fig. 3.** ENDF/B-VIII.0 total cross section for $YH_2$ (Brown et al., 2018).



**Fig. 4.** Net Signal to background for the ETTC.

the areal density must be split into two components: one for the area seen by the neutrons, and the other for the remainder area. Fortunately, the area seen by the neutron beam is well known from the collimator system.

One method of correcting the areal density relies on a constant density (and therefore constant hydrogen concentration) across the sample. Eq. (1) below shows how the average density, $\bar{\rho}$, is found as a function of sample mass (m), Area (A), and average thickness ($\bar{t}$). The average thickness was found by conducting thickness measurements across the entire area of the sample.

$$\bar{\rho} = \frac{m}{\bar{t} * A} \tag{1}$$

An average thickness of the sample for the interior region seen by the neutrons, $\bar{t}_1$, was measured. By utilizing Eq. (1) and the average thickness for the interior region of the sample, the areal density for the interior region seen by the neutrons could be found ($N_1$), as shown in Eq. (2). The atomic masses of yttrium and hydrogen were combined
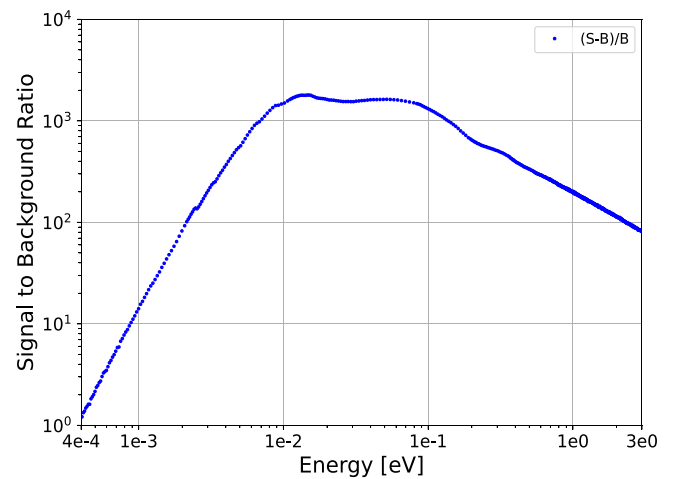
to form a molar mass of 90.770314 [g/mol] and 90.598984 [g/mol] for $YH_{1.85}$ and $YH_{1.68}$, respectively. An atomic mass of 88.905838 [g/mol] and 1.007825 [g/mol] were used for yttrium and hydrogen, respectively (de Laeter et al., 2003).

$$N_1 = \frac{m_1 * N_a}{M * A_1} = \frac{\bar{\rho} * \bar{t}_1 * N_a}{M} \tag{2}$$

Where:

   $m_1$, $A_1$: Sample mass and area corresponding to region 1

   $N_a$: Avogadro's number

   $M$: Molar Mass

A density of 4.2493 ± 0.0608 [g/cc] was found for the 2 mm, $YH_{1.85}$ sample by performing a thorough thickness mapping to find an average thickness for the sample. It should be noted that the density of the 2 mm, $YH_{1.85}$ sample is in very good agreement with the density of the 5 mm, $YH_{1.85}$ sample, which was found to be 4.2492 ± 0.0126. To find $\bar{t}_1$, a thickness mapping was performed to find the average thickness inside a diameter of 4.7625 cm that corresponds to the diameter of the collimator system.
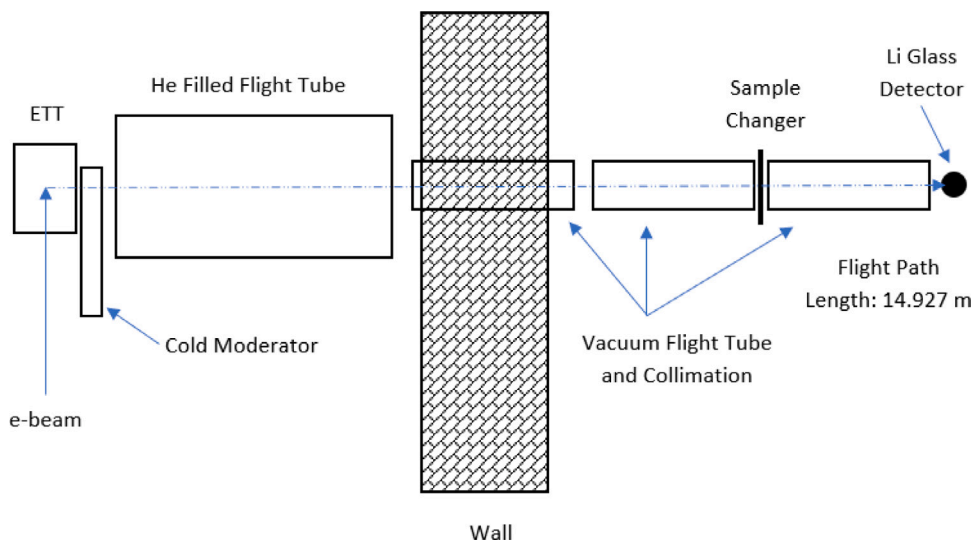
**Fig. 5.** Side view of neutron flight path for ETTC.

**Table 1**
Sample dimensions.

| Sample | Diameter [cm] | Mass [g] | Areal density [atom/barn] |
|---|---|---|---|
| 5 mm, $YH_{1.85}$ | 4.974 ± 0.001 | 43.5656 ± 0.0004 | 0.014870 ± 0.000003 |
| 2 mm, $YH_{1.85}$ | 4.983 ± 0.001 | 17.5499 ± 0.0002 | 0.005864 ± 0.000102 |
| 5 mm, $YH_{1.68}$ | 4.945 ± 0.001 | 43.2684 ± 0.0004 | 0.014970 ± 0.000004 |
| 2 mm, $YH_{1.68}$ | 4.953 ± 0.001 | 16.2584 ± 0.0002 | 0.0056090 ± 0.0000006 |

This calculation of the areal density for non-uniform samples depends on a constant density, which corresponds to a uniform hydrogen concentration in the case of yttrium hydride. Unfortunately, correcting for non-uniform sample thickness results in significantly higher uncertainty for the 2 mm, $YH_{1.85}$ sample as uncertainties (characterized by the standard deviation on the average) in the thickness measurements are relatively large. This increase in the overall uncertainty of the 2 mm, $YH_{1.85}$ sample due to the thickness measurement is accounted for in the areal density uncertainty, shown in Table 1. It should be noted that the other samples did not have this complication. In addition, all uncertainties on the areal density for each sample shown in Table 1 includes uncertainty from mass and diameter measurements.

These four samples were placed on the sample changer and measured for one week. Fig. 6 shows one of the 5 mm samples. Prior to experimentation, a chemical impurity analysis was performed on the yttrium hydride samples, shown in Table 2. The impurity analysis focused on elemental impurities with a large thermal cross section, such as gadolinium, and found that these impurities were in sufficiently small concentrations to have a negligible impact on the measured cross section.

While neither oxide nor nitride formation were assessed in the chemical impurity analysis, previous XRD measurements showed no noticeable oxide formation following YHx sample fabrication (Hu et al., 2020). It should be noted that a very slight black residue was noticed on all of the samples upon arrival. While this black residue was likely from nitrogen attack on the sample, it was wiped off of all of the samples prior to experimentation and mass measurement. After the completion of the transmission measurements, no additional residue was noticed.

It should be noted that a tantalum impurity was observed during the cross section measurements in the yttrium hydride samples that was not seen in the chemical impurity analysis, as evidenced by the presence of 4.28 eV and 10.34 eV resonances. This tantalum impurity was found to have a concentration of about 1500 ppm. At this concentration, the impact of the tantalum outside of the two resonances is negligible

compared to the cross section of yttrium hydride. In addition, the coherent elastic scattering contribution from known constituents ($\alpha$-phase yttrium metal) and possible impurities ($\epsilon$-phase $YH_3$, yttrium oxide, yttrium nitride) has not been fully assessed, but is expected to be very small due to the small concentrations present.

## 4. Calculation of cross section and associated uncertainty

### 4.1. Cross section

In a neutron transmission experiment, the actual quantities measured are the count rates with a given sample in beam and the sample out of beam, or open sample. The measured count rate and the background count rate for the open and the $YH_{1.85}$, 5 mm samples can be seen in Fig. 7 below. Here it can be seen that the background rate for the $YH_{1.85}$, 5 mm sample is well below the $YH_{1.85}$, 5 mm sample count rate until about 1 meV, where the count rate spectrum begins to curve. This is due to a low signal-to-background ratio at this energy for the $YH_{1.85}$, 5 mm sample. By contrast, the open sample spectrum does not begin to curve until right around 0.4 meV. It should be noted that open and $YH_{1.85}$, 5 mm sample count rates shown in Fig. 7 are not background subtracted. Additionally, the sharp edges seen in both samples at low energies are Bragg edges from the in-beam lead. However, the effects of these Bragg edges are washed out in transmission since the same amount of lead was present in all measured samples.

The count rates of the open and the sample are normalized using beam-intensity monitors, background subtracted and dead-time corrected to find the sample transmission. Eq. (3) shows that transmission for each TOF channel, $T(t_i)$, is found by taking the ratio of the count rate in the sample, $C_S(t_i)$, over the count rate in the open, $C_O(t_i)$ (Danon, 1993).

$$T(t_i) = \frac{(C_s(t_i) - K_s B(t_i) - B0_s)}{(C_o(t_i) - K_o B(t_i) - B0_o)} \tag{3}$$

Where

$B(t_i)$ [cps]: Fitted time-dependent background.

$B0_s, B0_o$ [cps]: Constant background in sample and open.

$K_s, K_o$: Time-dependent background normalization factors for sample and open.

In transmission there are two background components for each sample: a constant background, B0, and a time-dependent background, $B(t_i)$. The constant background was present at all times and comes
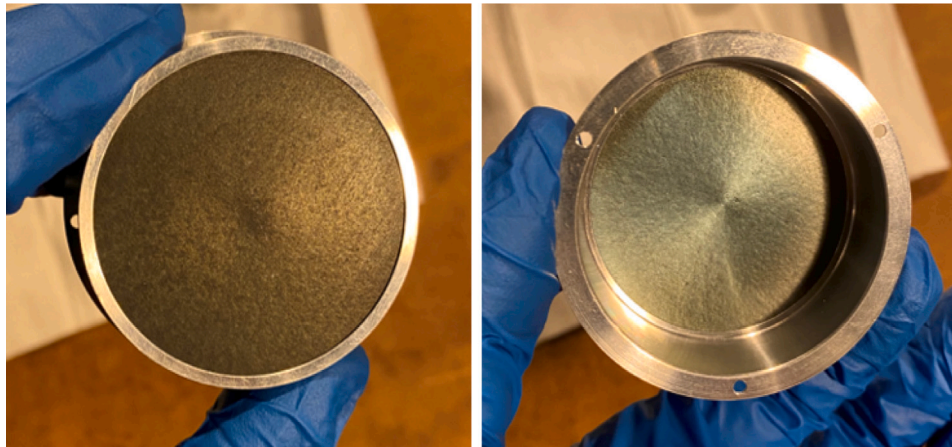
**Fig. 6.** Yttrium hydride sample.

**Table 2**
Chemical impurity analysis.

| Sample | YH$_{1.68}$ | YH$_{1.68}$ | YH$_{1.85}$ | YH$_{1.85}$ |
| --- | --- | --- | --- | --- |
| Thickness | 5 mm | 2 mm | 5 mm | 2 mm |
| | Wt% | Wt% | Wt% | Wt% |
| Silicon | 0.024 ± 0.001 | 0.017 ± 0.001 | 0.019 ± 0.001 | 0.018 ± 0.001 |
| Iron | 0.037 ± 0.001 | 0.0062 ± 0.0005 | 0.0096 ± 0.0005 | 0.0059 ± 0.0005 |
| Aluminum | 0.0073 ± 0.0005 | 0.0009 ± 0.0005 | 0.0013 ± 0.0005 | 0.0006 ± 0.0005 |
| Manganese | 0.017 ± 0.001 | 0.0010 ± 0.0005 | 0.0013 ± 0.0005 | 0.0011 ± 0.0005 |
| Nickel | <0.0005 ± 0.0005 | <0.0005 ± 0.0005 | 0.0009 ± 0.0005 | 0.0007 ± 0.0005 |
| Gadolinium | <0.002 ± 0.002 | <0.002 ± 0.002 | <0.002 ± 0.002 | <0.002 ± 0.002 |
| Samarium | <0.002 ± 0.002 | <0.002 ± 0.002 | <0.002 ± 0.002 | <0.002 ± 0.002 |
| Europium | <0.002 ± 0.002 | <0.002 ± 0.002 | <0.002 ± 0.002 | <0.002 ± 0.002 |
| Calcium | 0.033 ± 0.002 | 0.26 ± 0.01 | 0.18 ± 0.01 | 0.33 ± 0.01 |
| Fluoride | 0.59 ± 0.01 | 0.64 ± 0.01 | 0.68 ± 0.01 | 0.70 ± 0.01 |
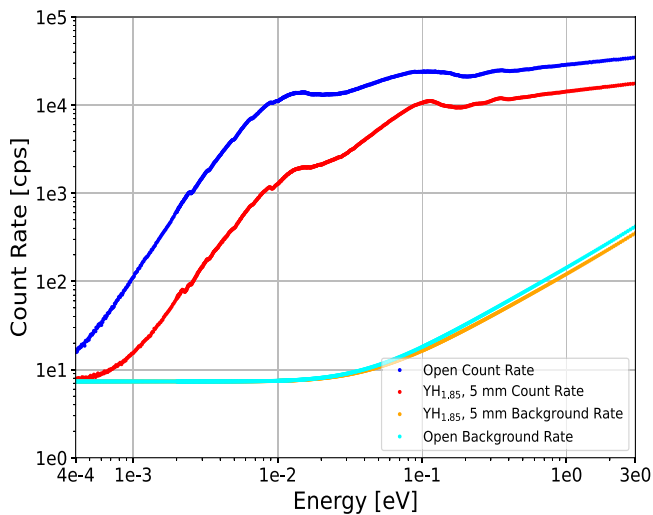


**Fig. 7.** Count rates for the open and the YH$_{1.85}$, 5 mm sample and its background.

from many sources during LINAC operations. The time-dependent background comes from off-time neutrons and neutrons that leak around the collimation system. The off-time neutrons were characterized using indium and cadmium notch filters in dedicated background runs in accordance with the double-notch (black resonance) method (Syme, 1982). In addition, the double-notch method was also applied at the end of the TOF data collection in these dedicated background runs to characterize the constant background present for each sample.

Eq. (4) shows how the total cross section was calculated from the measured transmission, $\sigma_{t,measured}(t_i)$. Here $N$ represents the measured

areal density for a given sample.

$$\sigma_{t,measured}(t_i) = \frac{-1}{N} * ln(T(t_i)) \, [barns] \tag{4}$$

Eq. (5) relates a neutron time of arrival, t [μs], to its non-relativistic energy, E [eV], for a well known flight path, L [m], through a constant value, K, of 72.29824 $\left[\frac{\sqrt{eV}\,\mu s}{m}\right]$. Since the TOF clock starts before neutrons are produced in the target, a t0 [μs] value representative of when the neutron burst originated needs to be subtracted from the measured neutron time of arrival, t. This t0 value was assessed to be 3.072 μs by measuring the time of flight for the burst of gamma rays produced when the electron pulse first interacts with the target, corrected for the flight time of the photons.

$$E = \left(\frac{KL}{t - t0}\right)^2 \, [eV] \tag{5}$$

### 4.2. Associated uncertainty

In transmission, there are two categories of uncertainty: statistical and non-statistical. The sources of statistical uncertainty stem from the counts of the thermal neutron detector as it applies to a sample and the counts of the monitor detector system as it applies to normalizing the sample counts to a beam intensity. Non-statistical uncertainty in transmission is dominated by how well the monitor detector system tracks changes in the beam intensity seen by the thermal neutron detector over the entire course of the experiment. For the various YHx samples, the contribution of monitor tracking to the uncertainty in transmission was found to be approximately 0.75% for each sample.

Typically, the statistical uncertainty in the transmission, $\Delta T_{stat}(t_i)$, is found by propagating statistical uncertainty from all sources and assuming that they are all independent, as shown in Eq. (6) (Danon,

1993).

$$\left(\frac{\Delta T_{stat}(t_i)}{T(t_i)}\right)^2 = \left(\frac{\Delta C_s(t_i)}{R_s(t_i)}\right)^2 + \left(\frac{\Delta C_o(t_i)}{R_o(t_i)}\right)^2 + \left(\frac{\Delta B0_s}{R_s(t_i)}\right)^2 + \left(\frac{\Delta B0_o}{R_o(t_i)}\right)^2$$
$$+ \left(\frac{K_o}{R_o(t_i)} - \frac{K_s}{R_s(t_i)}\right)^2 \Delta B(t_i)^2 \tag{6}$$

Where

$R_s(t_i)$ [cps] $= C_s(t_i) - K_s B(t_i) - B0_s$

$R_o(t_i)$ [cps] $= C_o(t_i) - K_o B(t_i) - B0_o$

$\Delta C_o(t_i), \Delta C_s(t_i)$: Uncertainty in open, sample count rate

$\Delta B0_o, \Delta B0_s$: Uncertainty in open, sample constant background

$\Delta B(t_i)$: Uncertainty in time-dependent background

In order to more accurately account for all sources of uncertainty, the transmission equation, given by Eq. (3), was modified to include monitor normalization factors. Eq. (7) shows this modification, where $F_s$, $F_o$, and $F_B$ are the monitor normalization factors for the sample, open and time-dependent background, respectively. It is important to note that all of these normalization factors are equal to 1, thereby making Eqs. (3) and (7) equivalent, but their associated uncertainty is propagated to the overall uncertainty of transmission.

$$T(t_i) = \frac{F_s(C_s(t_i) - B0_s) - F_B K_s B(t_i)}{F_o(C_o(t_i) - B0_o) - F_B K_o B(t_i)} \tag{7}$$

To form a covariance matrix and account for correlations in the data, the derivative of transmission with respect to each variable found in Eq. (7) was calculated. A separate covariance matrix was first formed for the statistical and systematic variables from their derivatives and associated uncertainties. For the systematic covariance matrix, a covariance matrix created during the time-dependent background shape fitting served as the basis matrix. These two covariance matrices were then added together to form a final, full covariance matrix. For more information concerning this method, see the discussion of uncertainty and correlation in Brown (2019). It should be noted that the count rate in the sample and open in Eq. (7) are categorized as statistical variables, while all other variables are categorized as systematic.

This final, full covariance matrix accounts for all quantifiable experimental sources of uncertainty. Fig. 8 below shows the correlation matrix for transmission of the 2 mm YH$_{1.68}$ sample from 0.0005–3 eV. Here it can be seen that the data is highly correlated except at very low energies. This correlation arises from the monitor tracking uncertainty dominating the total uncertainty for transmission. If the monitor tracking error is ignored, then there is little to no correlation. At very low energies, the effects of correlations on the total uncertainty diminishes due to increasing statistical uncertainty on the sample counts.

Taking the diagonal of the covariance matrix provides uncertainty values on transmission that can then be propagated to cross section. Jumps in the transmission uncertainty are due to time compression points. The uncertainty in the measured total cross section as given in Eq. (4) is a function of the total uncertainty in transmission, $\Delta T(t_i)$, and uncertainty in the areal density, $\Delta N$, as seen in Eq. (8). In general, the creation of a covariance matrix increases the total uncertainty in transmission since systematic sources of uncertainty are combined with the statistical uncertainty from Eq. (6).

$$\left(\frac{\Delta \sigma_{t,measured}(t_i)}{\sigma_{t,measured}(t_i)}\right)^2 = \left(\frac{\Delta N}{N}\right)^2 + \left(\frac{\Delta T(t_i)}{T(t_i)}\right)^2 \left(\frac{1}{ln(T(t_i))}\right)^2 \tag{8}$$

## 5. Results and discussion

Once the background was properly determined and subtracted from the measured count rate using Eq. (3), the calculation of neutron cross section and its associated uncertainty could be determined. Fig. 9 shows a comparison of the measured yttrium hydride total cross section with two different evaluations. The current ENDF/B-VIII.0 evaluation for H-in-YHx was combined with the Zerkle & Holmes evaluation for Y-in-YHx at H/Y ratios of 1.85 and 1.68. This combined ENDF/B-VIII.0 and Z&H evaluation was processed with both NJOY (Macfarlane

et al., 2017) and NDEX (Sutton et al., 2007). In addition, the ORNL evaluations for H-in-YHx and Y-in-YHx were processed with NJOY and combined at H/Y ratios of 1.85 and 1.68. The Z&H and ORNL evaluations for Y-in-YHx are shown here due to the inclusion of the coherent elastic contribution, while the current ENDF/B-VIII.0 evaluation for Y-in-YHx assumes all scattering is incoherent. For all evaluations shown, impurities were approximated as free gas and $\alpha$-phase yttrium was approximated as $\delta$-phase Y-in-YH$_2$. In general, the cross section agrees very well between the experimental data and the two evaluations shown. Structure in the experimental data at low energies is Bragg effects from the yttrium in yttrium hydride, where a slight disagreement concerning size and location of the Bragg edges exists between the evaluations and the experimental data.

It should be noted that error bars are plotted for all 5 mm experimental data, but are difficult to see at most energies due to their small magnitude. These error bars represent the diagonal of the covariance matrix calculated for each sample. All data points shown for all yttrium hydride experimental results have an uncertainty of less than 5%. Additionally, while the uncertainty of the areal density for the YH$_{1.85}$, 2 mm sample is included in the cross section, the primary purpose of this sample is to validate the cross section structure of the YH$_{1.85}$, 5 mm sample.

Between 0.1 and 1 eV there are oscillations in the experimental data that are shown more closely in Fig. 10. These oscillations stem from multi-phonon scattering in the YHx, and affect the inelastic scattering cross section in hydrogen bound in yttrium hydride as shown in Fig. 1. However, as the neutron energy increases the frequency of these experimental oscillations becomes increasingly out of sync with both the ENDF/B-VIII.0 + Z&H evaluation and the ORNL evaluation. This oscillation misalignment is partially explained by a deficiency in the NJOY (THERMR) energy meshing algorithm when processing metal hydrides (Wormald et al., 2020). When the ENDF/B-VIII.0 + Z&H evaluation is processed with the NDEX code suite, the real structure of the oscillations present in the evaluation is visible. Though even with the more rigorous processing of the evaluations, discrepancies are still present. While anharmonic behavior in the yttrium hydride phonon modes occurs even at room temperature, its impact on thermal neutron scattering cross sections is not fully understood (Zhang et al., 2021). In addition, impurities present in the samples or variations in microcrystal structure can disrupt the ideal phonon spectrum of yttrium hydride, resulting in deviations between the experiment and the evaluation. It should be noted that deficiencies in both NJOY (LEAPR) and NDEX need to be resolved in order to properly account for anharmonic behavior during TSL generation (Chapman et al., 2021).

Other experimental data exists for yttrium hydride, but this data only addresses the hydrogen cross section in the 0.05–0.75 eV energy range. Vorderwisch and Wasserroth (1969) measured the hydrogen scattering cross section per hydrogen for YH$_{1.90}$, while Brand (1970) found the hydrogen total cross section per hydrogen for YH$_{1.88}$. In order to make an accurate comparison to the measured total cross section of YH$_{1.85}$, each data set was scaled to H/Y = 1.85, with ENDF/B-VIII.0 hydrogen capture cross section added to V&W, and data from the Z&H Y-in-YHx evaluation added to both V&W and Brand. A comparison to the RPI measured cross section for YH$_{1.85}$ and the ENDF/B-VIII.0 + Z&H evaluation is made in Fig. 11. Here, good agreement between the RPI and V&W data is seen below 0.1 eV, and decent agreement between the RPI and Brand data is seen above 0.15 eV.

At lower energies, the Bragg edges in the yttrium component of YHx are easily seen, as shown in Fig. 12. There is excellent agreement between the two YH$_{1.85}$ samples over this energy range, while a small disagreement between the two YH$_{1.68}$ samples from 0.002–0.01 eV is observed. Given that the majority of the uncertainty for the two samples in this energy region is systematic, this disagreement is believed to represent real structural differences between the two samples. The amplitude differences of the Bragg edge peaks around 0.002 eV and 0.009 eV suggest that differences in the crystal structure of the yttrium hydride (i.e., grain size, degree of crystallinity, dislocations) are present
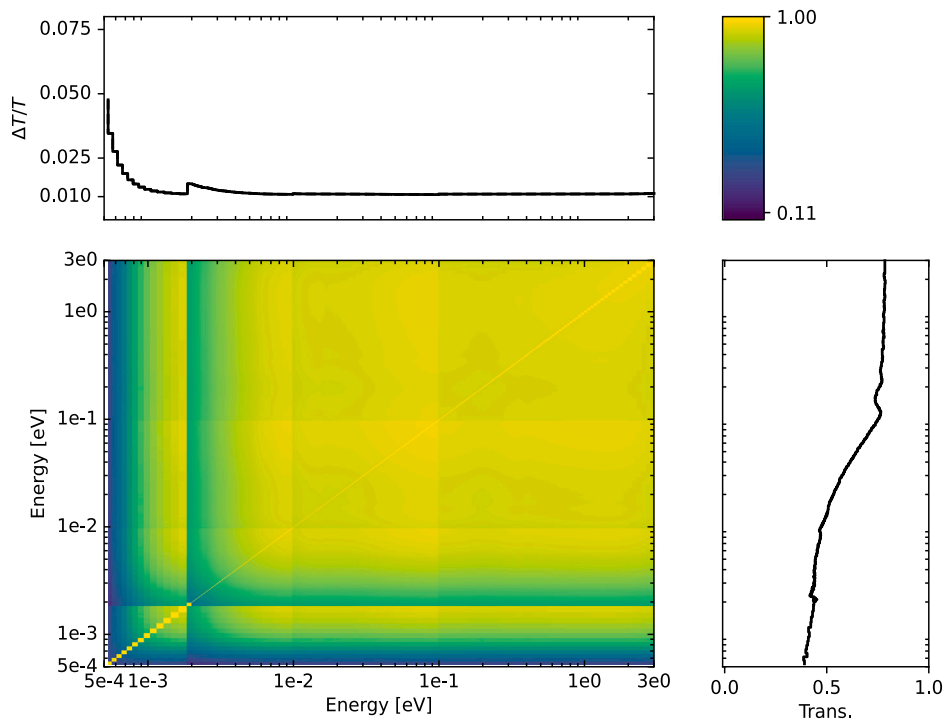
**Fig. 8.** Correlation matrix for 2 mm YH$_{1.68}$ from 0.0005–3 eV.
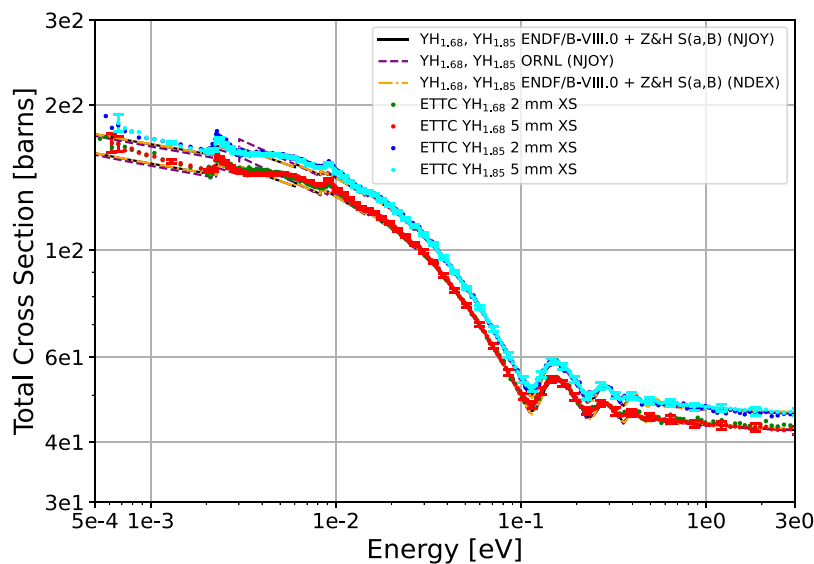


**Fig. 9.** Total cross section for yttrium hydride with calculated uncertainty from all quantifiable sources. Generally good agreement is seen between all evaluated data and the RPI experimental data over the entire thermal energy range for both YH$_{1.68}$ and YH$_{1.85}$.

between the two samples (Dijulio et al., 2020). However, disruptions to the crystal lattice structure, and the resulting alteration of the yttrium coherent elastic scattering component, caused by impurities present in one or both of the samples could also contribute to this observed discrepancy.

Below 0.015 eV there are disagreements between the experimental data sets and the evaluations at both hydrogen concentrations. These disagreements occur both from the energy locations and the cross section amplitudes of the Bragg edges. After the last Bragg edge (approximately 0.002 eV), the incoherent inelastic cross section of yttrium hydride can be seen clearly. The small discrepancy seen below 0.002 eV between the experimental data and the evaluations is believed to be from the approximation of $\alpha$-phase yttrium metal as $\delta$-phase Y-in-YH$_2$.

This is evidenced by closer agreement between experimental results and evaluations for YH$_{1.85}$ than YH$_{1.68}$.

In order to better understand the differences between the evaluated data and the RPI experimental data, a C/E plot was created, shown in Fig. 13. Experimental data from the YH$_{1.85}$, 5 mm and YH$_{1.68}$, 5 mm samples were used for these comparisons. From Fig. 13, the largest deviations between the evaluated data and the RPI experimental data occur below 0.01 eV.

Work has been performed to characterize the resolution of the thermal neutron producing target system, with the system easily resolving resonances from tantalum present at 4.28 and 10.34 eV, as well as Bragg edges that occur from beryllium present below 10 meV. Thus the structure seen in the yttrium hydride samples is real, and not a
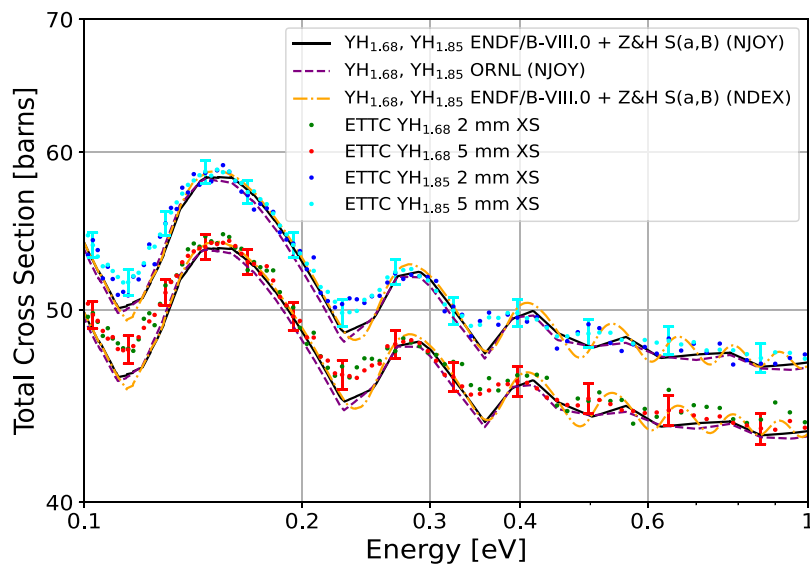
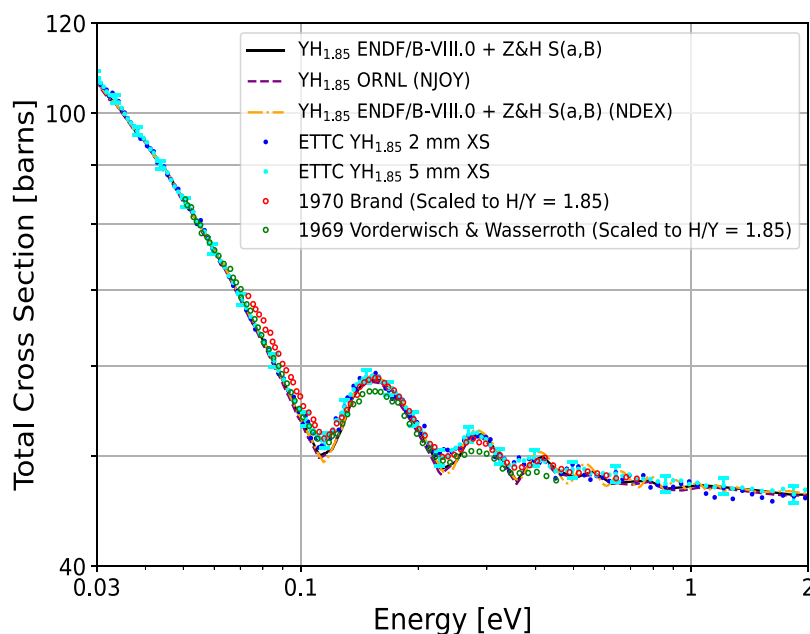**Fig. 10.** Total cross section yttrium hydride from 0.1–1 eV.



**Fig. 11.** Total cross section for yttrium hydride from 0.03–2 eV. Data from Brand and V&W are scaled to YH$_{1.85}$. ENDF/B-VIII.0 hydrogen capture cross section is added to V&W, while Z&H yttrium in YHx total cross section is added to both.

smearing of the experiment due to resolution from the moderator system. Additionally, all experimental data shown has a total cross section uncertainty less than 5%, with the maximum uncertainty occurring at the lowest energy point (0.5 meV) for all samples. These measurements were performed at room temperature.

It is important to mention that the uncertainty on the H/Y ratio for each sample was never measured. However, the transmission measurements were used to probe the magnitude of the uncertainty on the H/Y ratio. The results of these uncertainty probes strongly suggested that the uncertainty was less than 1% on the H/Y ratio for each sample.

**6. Conclusion**

Using a well known flight path at the RPI LINAC, four total cross section measurements were performed for yttrium hydride from 0.0005–3 eV, representing the first total cross section measurements

that encompass the entire thermal region. These cross section measurements were used to validate the ORNL and ENDF/B-VIII.0 + Z&H thermal scattering library evaluations at H/Y ratios of 1.85 and 1.68. Generally good agreement was found between the experimental data and the evaluations. Some structural differences were discovered at lower energies in the form of Bragg edges and a misalignment of the hydrogen oscillations is present at higher energies.

It should be noted that while these evaluations performed well for yttrium hydride fabricated with the bulk hydridation methods, differences could exist for yttrium hydride fabricated through sintering at the same hydrogen concentration. Additionally, as the hydrogen concentration falls, more yttrium is present in the form of $\alpha$-phase yttrium metal instead of $\delta$-phase Y in YH$_2$. This will alter the scattering cross section of yttrium hydride, specifically the size and location of the Bragg edges. Therefore, future work includes the exploration of the effects of different fabrication methods and the presence of large
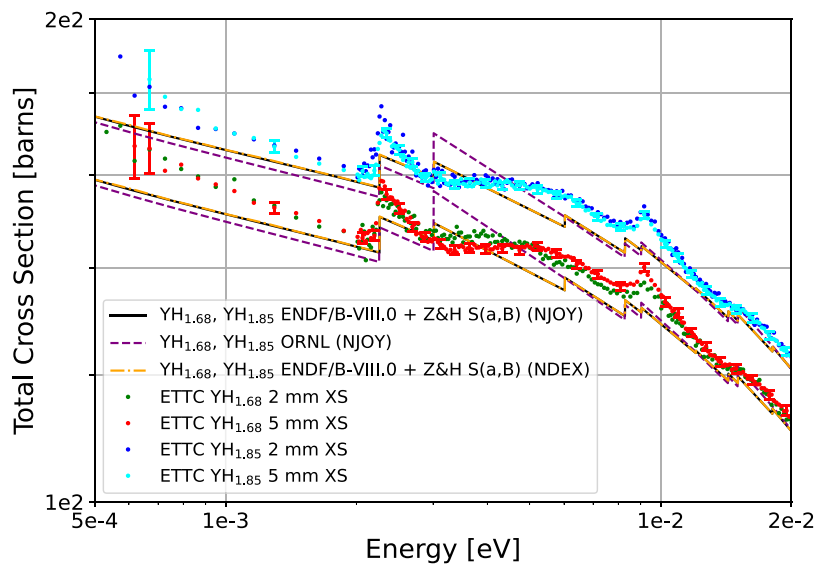
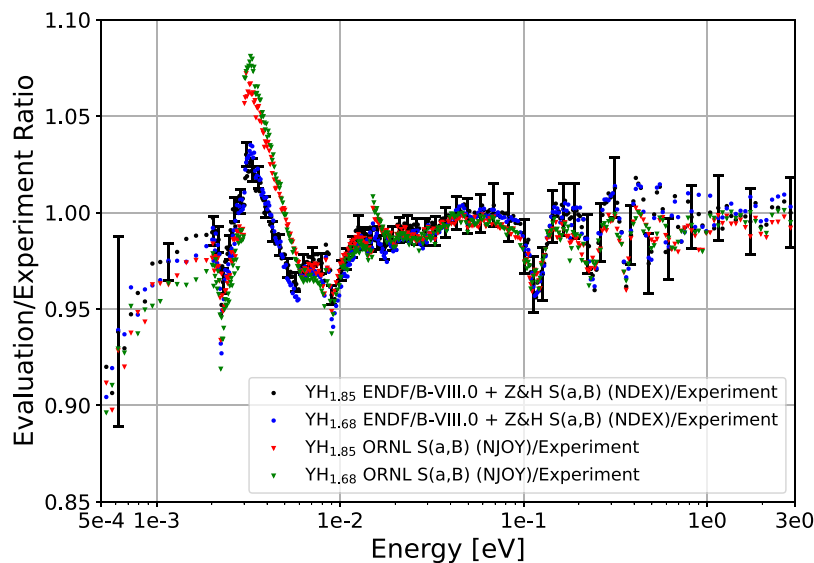**Fig. 12.** Total cross section for yttrium hydride from 0.0005–0.02 eV.



**Fig. 13.** Evaluation to RPI experiment ratio for the ORNL TSL evaluation processed with NJOY and the ENDF/B-VIII.0 + Z&H TSL evaluation processed with NDEX for $YH_{1.85}$ and $YH_{1.68}$. The experimental data from the $YH_{1.85}$, 5 mm sample and the $YH_{1.68}$, 5 mm sample were used in this comparison. Error bars are only plotted for the $YH_{1.85}$ ENDF/B-VIII.0 + Z&H TSL/Experiment ratio for plot visibility, and stem from the error associated with the $YH_{1.85}$, 5 mm sample.

amounts of $\alpha$-phase yttrium metal on the total cross section of yttrium hydride. Additional transmission measurements should be conducted for samples with a higher purity and a more thorough characterization of residual impurities and crystal structure. These measurements would allow for a better understanding of the impact of impurities and crystal structure on the total cross section, particularly in the Bragg edge and hydrogen oscillation energy regions. Due to the decrease of anharmonic behavior at low temperatures, transmission measurements performed with yttrium hydride samples at low temperature would assist in determining the impact of anharmonic behavior on the neutron total cross section.

**Declaration of competing interest**

The authors declare that they have no known competing financial interests or personal relationships that could have appeared to influence the work reported in this paper.

**Data availability**

Data will be made available on request.

# References

Brand, K., 1970. Total neutron cross sections of chemically bound protons and deuterons in some metal hydrides and deuterides. Germany. URL https://www.osti.gov/biblio/4378077.

Brown, J.M., 2019. Measurements, evaluation, and validation of Ta-181 resolved and unresolved resonance regions. In: Submission for Doctor of Philosophy. Rensselaer Polytechnic Institute.

Brown, D., Chadwick, M., Capote, R., Kahler, A., Trkov, A., Herman, W., Sonzogni, A., Danon, Y., Carlson, A., Dunn, M., Smith, D., Hale, G., Arbanas, G., Arcilla, R., Bates, C., Beck, B., Becker, B., Brown, F., Casperson, R., Conlin, J., Cullen, D., Descalle, M., Firestone, R., Gaines, T., Guber, K., Hawari, A., Holmes, J., Johnson, T., Kawano, T., Kiedrowski, C., Koning, A., Kopecky, S., Leal, L., Lestone, J., Lubitz, C., Marquez, J., Mattoon, C., McCutchan, E., Mughabghab, S., Navratil, P., Neudecker, D., Nobre, G., Noguere, G., Paris, M., Pigmi, M., Plompen, A., Pritychenko, B., Pronyaev, V., Roubtsov, D., Rochman, D., Romano, P., Schillebeeckx, P., Simakov, S., Sin, M., Sirakov, I., Sleaford, B., Sobes, V., Soukhovitskii, S., Stetcu, I., Talou, P., Thompson, I., van der Marck, S., Welser-Sherrill, S., Wiarda, D., White, M., Wormald, J., Wright, R., Zerkle, M., Aerovnik, G., Zhu, Y., 2018. ENDF/B-VIII.0: the 8th major release of the nuclear reaction data library with CIELO-project cross sections, new standards and thermal scattering data. Nucl. Data Sheets 148, 1–142.

Chapman, C.W., Ramic, K., Hu, X., Brown, J.M., Arbanas, G., Kolesnikov, A.I., Abernathy, D.L., Daemen, L.L., Ramirez-Cuesta, A.J., Cheng, Y., Stone, M.B., Liu, L., Danon, Y., 2020. Thermal Neutron Scattering Evaluation of Yttrium Hydride (FY2020 Progress). Oak Ridge National Laboratory Report No. ORNL/TM-2020/1666, http://dx.doi.org/10.2172/1659577.

Chapman, C.W., Ramić, K., Hu, X., Brown, J.M., Arbanas, G., Kolesnikov, A.I., Abernathy, D.L., Daemen, L., Ramirez-Cuesta, A.T.J., Cheng, Y., Stone, M.B., Liu, L.E., Danon, Y., 2021. Thermal neutron scattering measurements and modeling of yttrium-hydrides for high temperature moderator applications. Ann. Nucl. Energy 157, 108224. http://dx.doi.org/10.1016/j.anucene.2021.108224.

Danon, Y., 1993. Design and contruction of the RPI enhanced thermal neutron target and thermal cross section measurements of rare earth isotopes. In: Submission for Doctor of Philosophy. Rensselaer Polytechnic Institute.

de Laeter, J.R., Böhlke, J.K., Bièvre, P.D., Hidaka, H., Peiser, H.S., Rosman, K.J.R., Taylor, P.D.P., 2003. Atomic weights of the elements: Review 2000. Pure Appl. Chem. 75, 683–800.

Dijulio, D., Lee, Y., Muhrer, G., 2020. Impact of crystallite size on the performance of a beryllium reflector. J. Neutron Res. 22, 275–279.

Fritz, D., Danon, Y., 2020. A cold moderator for sub-thermal neutron flux enhancement at the RPI LINAC. In: 2020 ANS Winter Meeting. Vol. 123.

Fritz, D., Danon, Y., 2021. Enhancement of sub-thermal neutron flux through cold polyethylene. J. Neutron Res. 23 (2–3), 179–184. http://dx.doi.org/10.3233/JNR-210010.

Hu, X., Schappel, D., Silva, C.M., Terrani, K.A., 2020. Fabrication of yttrium hydride for high-temperature moderator application. J. Nucl. Mater. 539, 152335.

Hu, X., Terrani, K.A., 2021. Thermomechanical properties and microstructures of yttrium hydride. J. Alloys Compd. 867, 158992.

Macfarlane, R., Muir, D.W., Boicourt, R.M., Kahler, A.C., Conlin, J.L., 2017. The NJOY Nuclear Data Processing System, Version 2016. Tech. rep., Los Alamos National Laboratory, LA-UR-17-20093.

Ramić, K., Marquez Damian, J.I., Kittelmann, T., Di Julio, D.D., Campi, D., Bernasconi, M., Gorini, G., Santoro, V., 2022. NJOY+NCrystal: An open-source tool for creating thermal neutron scattering libraries with mixed elastic support. Nucl. Instrum. Methods Phys. Res. A 1027, 166227. http://dx.doi.org/10.1016/j.nima.2021.166227.

Shivprasad, A.P., et al., September 2020. Advanced Moderator Material Handbook. Tech. rep., Los Alamos National Laboratory, LA-UR-20-27683.

Sutton, T., Donovan, T., Trumbull, T., Dobreff, P., Caro, E., Griesheimer, D., Tyburski, L., Carpenter, D., Joo, H., 2007. The MC21 Monte Carlo transport code. In: American Nuclear Society Joint International Topical Meeting on Mathematics Computation and Supercomputing in Nuclear Applications Report No. LM-06K144. 2007.

Syme, D.B., 1982. The black and white-filter method for background determination in neutron time-of-flight spectrometry. Nucl. Instrum. Methods 198, 357–364.

Vorderwisch, P., Wasserroth, K., 1969. Total neutron-proton scattering cross section of yttrium hydride. Atomkernenergie 14, 370, (Sept.-Oct. 1969). URL https://www.osti.gov/biblio/4722662.

Werner, C.J., Bull, J.S., Solomon, C.J., Brown, F.B., McKinney, G.W., Rising, M.E., Dixon, D.A., Martz, R.L., Hughes, H.G., Cox, L.J., Zukaitis, A.J., Armstrong, J.C., Forster, R.A., Casswell, L., 2018. MCNP-6.2 Release Notes, LA-UR-18-20808. Tech. rep., Los Alamos National Laboratory, http://dx.doi.org/10.2172/1419730.

Wormald, J., Thompson, J., Trumbull, T., 2020. Implementation of an adaptive energy grid routine in NDEX for the processing of thermal neutron scattering cross sections. Ann. Nucl. Energy 149, 107773. http://dx.doi.org/10.1016/j.anucene.2020.107773.

Zerkle, M.L., Holmes, J.C., Wormald, J.L., 2021. Re-evaluation of the TSL for yttrium hydride. EPJ Web Conf. 247, 09015. http://dx.doi.org/10.1051/epjconf/202124709015.

Zhang, J., Cheng, Y., Kolesnikov, A.I., Bernholc, J., Lu, W., Ramirez-Cuesta, A.J., 2021. Study of anharmonicity in Zirconium hydrides using inelastic neutron scattering and Ab-initio computer modeling. Inorganics 9 (2021), http://dx.doi.org/10.3390/inorganics9050029.

Zhu, Y., Hawari, A.I., 2018. FLASSH, "Full Law Analysis Scattering System Hub". In: Proceedings of PHYSOR 2018, Cancun, Mexico, April 22-26 (2018).